XMM-Newton Calibration Technical Note

XMM-SOC-CAL-TN-0030
issue 7.9

Status of the RGS Calibration

Compiled by R. González-Riestra, on behalf of the RGS consortium

July 20, 2020

Contents

1 Introduction

The two high-resolution RGS instruments aboard the XMM-Newton Observatory have been operating since first light a few weeks after launch in 1999. The set of CCF calibration files that describes the instruments has undergone significant development since then to include in particular time-variable empirical effective area corrections for RGS 1 and RGS 2 over the 6-38 Å bandwidth. As described in more detail below, these corrections were derived independently for the RGS based on reasonable assumptions concerning the spectral form of a few well-known X-ray sources, and have had the effect of greatly improving the agreement between RGS and the EPIC instruments, the differences between which now conservatively stand at a few percent.

In addition to the slowly-changing, wavelength-dependent changes in the sensitivity of the RGS, one CCD assembly of the nine in each RGS failed early in the mission because of electronics problems. These were RGS 1 CCD7 and RGS 2 CCD4, roughly covering the wavelength ranges 11-14 Å and 20-24 Å, respectively, in first order. Coverage of the wavelengths affected has been maintained by the built-in redundancy between RGS 1 and RGS 2 or between first and second order or both.

Concerning its high-resolution capabilities, measurements of wavelengths are accurate to better than about 6 mÅ. The dramatic reduction of the effects of radiation damage after the operating temperatures of RGS 1 and RGS 2 were lowered from -80°C to -110°C in November 2002 has been maintained. Otherwise the instruments continue to operate as well as before.

Table 1: Summary of the main characteristics of the XMM-Newton Reflection Grating Spectrometers in standard spectroscopy mode.

Calibrated bandwidth: 6 - 38 Å (0.33 - 2.07 keV)

	1st order	2nd order
Maximum effective area*	130 cm^2 at 15 Å	60 cm^2 at 10 Å
Spectral Resolution	250 at 15 Å	300 at 10 Å
Wavelength accuracy	6 mÅ	6 mÅ
* RGS 1+RGS 2		
	RGS 1	RGS 2
CCD integration time	0.6 s	1.2 s

Typical full-detector background rates	
6-8 Å	5 cts ks^{-1} $Å^{-1}$
8-27 Å	2 cts ks^{-1} $Å^{-1}$
27-34 Å	7 cts ks^{-1} $Å^{-1}$
34-38 Å	2 cts ks^{-1} $Å^{-1}$

The purpose of this document is to alert users to the quality of the instrumental calibrations developed so far in order to provide a proper context for the scientific interpretation of RGS data. Documents of varying levels of complexity are available to people interested in the details of the instrument's construction and behaviour: a summary of important instrumental parameters is shown below, a more thorough description of the instrument and the flight performance is given in [1] and [2], and detailed individual calibration documents, written mainly by instrument experts at SRON Utrecht, Columbia University and the XMM-Newton SOC, are available as shown by the list of

references at the end of this document.

The RGS deliver high spectral resolution for an effective area of typically 100 cm^2. The instrumental line width is weakly wavelength dependent with mean FWHM of about 70 mÅ and 50 mÅ in first and second order, respectively. Pending more detailed discussion below, the overall performance is summarised in Table 1.

2 The RGS Calibration

The instrument calibration is based on a physical model of the various instrument components:

- Mirror response (not part of this document)
- Grating response:
  - Reflectivity
  - Figure errors
  - Scattering
  - Alignment
  - Vignetting
- CCD detector response:
  - Quantum efficiency
  - Monochromatic pulse-height redistribution function
  - Transmission of the optical blocking filter
  - Charge transfer inefficiency (CTI)
  - Gain

During ground calibrations, these various components were calibrated and a physical model for each constructed and later verified in flight. Subsequent adjustments in the form of time-dependent and wavelength-dependent empirical corrections have been based on in-flight observations of specific sources.

The resulting knowledge of the instrument is encapsulated in the RGS CCF files shown in Table 2 with some important relevant general-purpose components. An extensive description of the instrument model is given in [1] and details may also be found in the XMM-Newton Users Handbook [3].

During routine operations, many instrumental parameters are monitored (detector contamination, detector gain, CTI evolution due to radiation damage, etc) and this leads to periodic modifications of the relevant RGS CCF components. It should be emphasised that new CCF components may be released at any time, not necessarily coordinated with new versions of the SAS or new issues of this document. Each new CCF component made publicly available is accompanied by a release note available at the XMM CCFs Release Notes Page with a name of the form XMM-CCF-REL-vvvv describing its relevance and applicability.

Purpose	CCF component	RGS 1 / 2	Release Note	Release Date
CCD event selection criteria	RGS[12]_ADUCONV	29 / 34	365	March 2019
CCD bad pixels	RGS[12]_BADPIX	38 / 32	370/292	March 2019 / August 2012
CCD readout parameters	RGS[12]_CLOCKPATTERNS	01 / 01	015	September 2000
CCD cool pixels	RGS[12]_COOLPIX	01 / 01	218	June 2006
Cross-dispersion PSF parameters	RGS[12]_CROSSPSF	04 / 04	142	December 2002
CCD CTI correction parameters	RGS[12]_CTI	15 / 16	345	January 2017
CCD dark response	RGS[12]_DARKFRAME	05 / 06	173	July 2004
CCD effective area correction factors	RGS[12]_EFFAREACORR	14 / 14	372	October 2019
CCD quantum efficiency correction factors	RGS[12]_EXAFS	05 / 05	212	June 2006
HK parameter selection criteria	RGS[12]_HKPARMINT	15 / 14	134	January 2017
RGS system geometry	RGS[12]_LINCOORD	08 / 08	081	June 2001
Dispersion PSF model parameters	RGS[12]_LINESPREADFUNC	05 / 05	275	December 2011
CCD readout parameters	RGS[12]_MODEPARAM	05 / 05	015	September 2000
CCD quantum efficiency physical model	RGS[12]_QUANTUMEF	15 / 16	215	June 2006
CCD energy response parameters	RGS[12]_REDIST	04 / 04	067	March 2001
Wavelength-scale correction parameters	RGS[12]_SAACORR	01 / 01	297	April 2013
Observed RGS background templates	RGS[12]_TEMPLATEBCKGND	06 / 08	261	April 2010
Henke X-ray absorption coefficient tables	XMM_ABSCOEFS	04	077	May 2001
Includes RGS Euler angles	XMM_BORESIGHT	30	375	February 2020
Includes assorted RGS data	XMM_MISCDATA	22	134	February 2000

Table 2: RGS components of the XMM-Newton CCF in July 2020. RGS[12] shows that there are separate files for RGS 1 and RGS 2. RGS-specific version numbers and Release Notes refer to the release applicable to the most recent data, while the general-purpose files refer to the latest versions relevant to the RGS. Please be aware that CCF releases generally occur more often than new editions of this document.

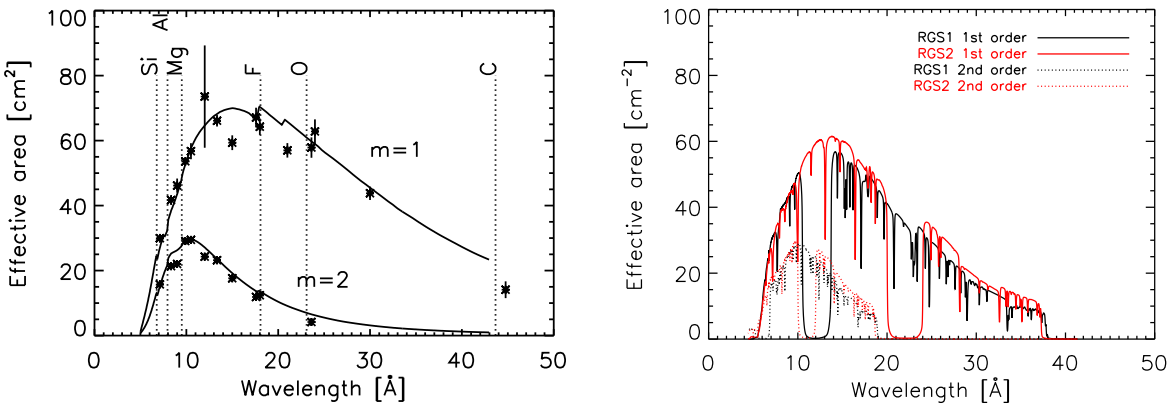

Figure 1: Left: Model of the effective area derived from ground calibrations with a number of measured data points [1]. Right: the CCF in-flight effective area of a typical observation for RGS 1 in black and RGS 2 in red [3]. Due to scattering the effective area has no sharp features.

2.1 Effective area

Knowledge of the effective area of the two RGS instruments comes from a combination of ground measurements and observations in flight. It has developed significantly since launch with the introduction of two particularly important additions to the calibration that was originally based on an end-to-end physical model of the whole system. Empirical corrections were first introduced in 2006, based on the assumed power-law form of blazar spectra [5], followed a year later by the recognition of wavelength-dependent sensitivity changes which are consistent with a build-up of hydrocarbon contamination on the cold CCD detector surfaces (see Sect. 2.1.2). The absolute accuracy of the effective area is estimated at 10%.

The overall characteristics of the effective area are illustrated in Fig. 1. Obvious features include the two failing CCD readout chains and the effect of a number of hot columns and pixels shown by narrow drops in the effective area. Instrumental Oxygen absorption is clearly visible near 23 Å. Less obvious instrumental features revealed on closer inspection include a shallow Al edge around 8.3 Å from the blocking filter on top of the CCDs and of Mg and F edges around 9.5 Å and 17.9 Å respectively from the MgF_2 isolation layer between the CCD and the blocking filter.

As a result of measurements in flight, the effective-area model incorporates these and a number of other corrections which apply to both RGS 1 and RGS 2 unless stated otherwise:

- Empirical corrections based on power-law blazar spectra
- Absorption in a contamination layer
- Dispersion-dependent corrections (RGS 1 only)
- Sensitivity adjustment of RGS 2 CCD2
- Instrumental Oxygen and MgF_2 features near 23 and 17.9 Å
- Empirical higher-order corrections.
- Empirical time and wavelength dependent correction.

2.1.1 Empirical effective-area corrections

The long-wavelength part of the RGS has been difficult to calibrate due to the scarcity of both suitable ground-based facilities and celestial X-ray standards. It has become clear that blazars have smooth spectra well characterised by power-laws subject to interstellar absorption in the RGS waveband. This was empirically supported by the fact that the RGS spectra calculated with earlier versions of the calibration could be corrected for interstellar absorption and power-law slope to reveal a universal form reflecting the shape of the effective area of the RGS instruments [5]. Empirical effective area corrections have been derived using measurements of Mkn 421 at different epochs during the mission and fitting a power-law models to the stable, well-calibrated part of the RGS waveband between 10 and 25 Å. Using the Crab as a reference for both power-law slope and normalisation [6], the extrapolation of the resulting models to long and short wavelengths has been used in comparison with the observed spectra to define correction factors. These correction factors are not thought to be time dependent but when combined with the contamination correction discussed immediately below, give rise to the time and wavelength-dependent tabulations in the `EFFAREACORR` CCF for the calculation of RGS response matrices.

At the shortest wavelengths, the underlying gratings model based on electromagnetic scalar theory breaks down at the small angles involved. This could not be compensated by measurements on the ground and so, at these shortest wavelengths, the empirical correction serves to compensate for the theoretical shortcomings.

2.1.2 Contamination correction

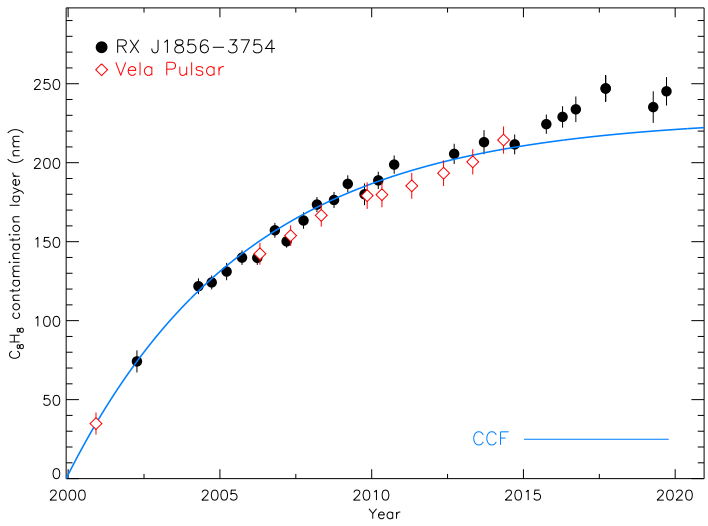

Figure 2: Thickness of the layer of Carbon contamination implied by differences in the RGS fluxed spectra of the neutron star RX J1856.6-3754 (black) and the Vela Pulsar (red). An exponential fit accounts in the CCF for the time-variable part of the model of the RGS effective area.

The RGS sensitivity has been decreasing at long wavelengths due almost certainly to the appearance of a layer of contamination on the CCDs. The layer was initially modelled as linearly increasing in thickness [7], with a slower rate of increase after a few years, as shown in Fig. 2 [8]. An exponential law is used to extrapolate into the future.

As shown in the Figure, the estimations of the depth of the contaminating layer are deviating from the predictions over the last few years. There are indications that this apparent increment of the contamination is due, at least partly, to a decrease in effective area over most of the RGS spectral range, that cannot be explained by contamination by Hydrocarbons.

2.1.3 RGS 1 dispersion-dependent correction

Data of calibration sources obtained early in the mission showed unexpected systematic differences between RGS 1 and RGS 2, with RGS 1 20% less efficient at larger dispersion angle, β, than RGS 2. Although not entirely satisfactory in physical terms, this could be explained by additional blocking of the beam halfway between the gratings and the detectors - although the required mismatch of the optical blocking shield by 5 cm in one of the two instruments would seem unrealistic. In any case, an empirical β-dependent correction ranging from 1.00 at β=0.038 rad (6.5 Å for first order) to 1.25 at β=0.075 rad (37.7 Å for first order) has been derived and is applied during SAS data processing [9].

2.1.4 Sensitivity of RGS 2 CCD2

For smooth continuum sources, comparison of the count rate of RGS 2 CCD2 with its neighbouring CCDs 1 and 3, and with RGS 1 CCD2 shows its sensitivity is about 10% lower than expected, likely due to an extra absorbing layer deposited during the manufacturing process. In order to ensure a smooth wavelength-dependent effective area, of various possibilities for an extra passive absorption layer to account for the lower sensitivity of this CCD, a 40 nm layer of SiO_2 gives the best description [10].

2.1.5 Instrumental absorptions

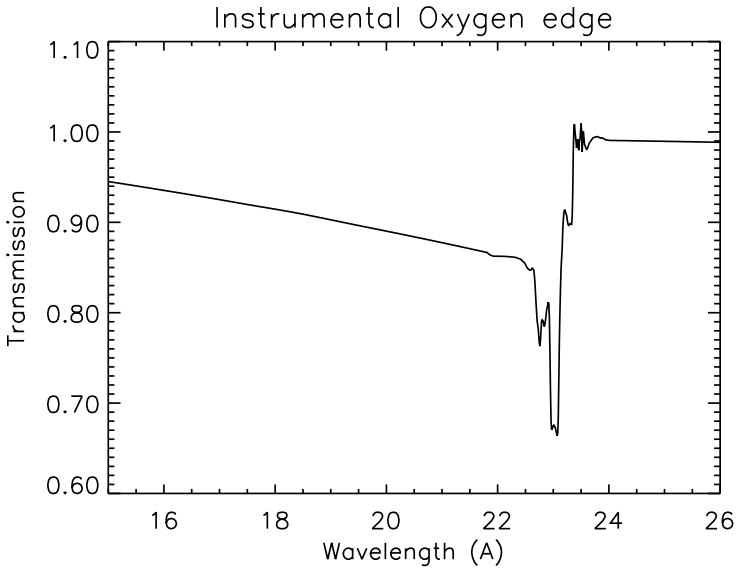

Figure 3: The effect of an additional Oxygen layer on the detectors as determined by comparison of sources of varying interstellar column densities.

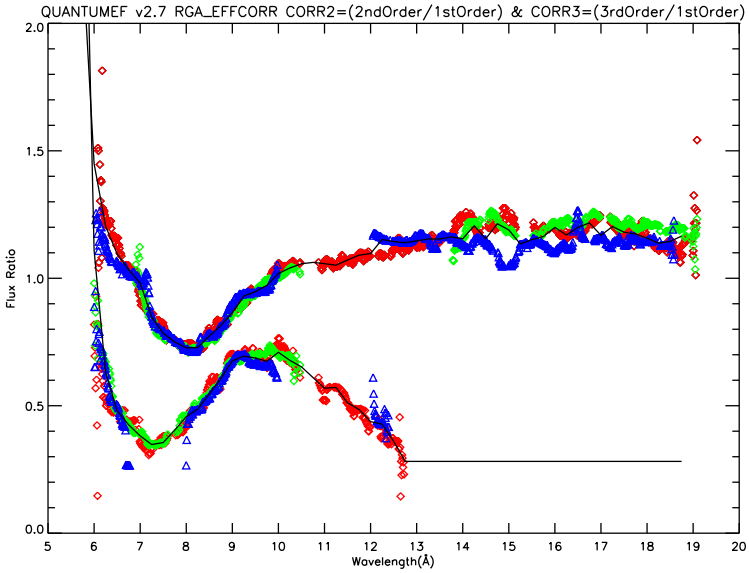

Figure 4: Corrections for second order (above) and third order (below) for the RGS instruments, shown with the solid-line approximations used in the CCF. RGS 1 before and after the loss of data from CCD7 is in red and green; RGS 2 in blue. See [13] for details.

Oxygen There is a significant reduction of about 25% in the effective area around the O-edge, roughly equivalent to a 30 nm layer of Al_2O_3. Details of this edge, including its fine structure, have been calibrated in flight using a number of sources with low and high column density to separate the detector response from interstellar absorption [11]. Fig. 3 gives both the global structure, that follows the Henke absorption coefficients, and the fine structure. The magnitude of the Oxygen layer on the detector has been confirmed by ground measurements on a flight-spare CCD. Nevertheless, the value of the oxide layer is rather large compared with the two native SiO_2 and Al_2O_3 oxide layers, each of assumed thickness 5 nm, so it is plausible that a layer of ice formed on the detector when they were cooled after launch.

Fluorine and Magnesium The 25 nm MgF_2 layer on the CCDs that isolates them from the optical Al filter gives rise to Mg and F absorption edges near 17.9 Å, see [12].

2.1.6 Higher-order corrections

Between the first and higher spectral orders, wavelength–dependent corrections have been introduced to enforce agreement. Identical correction factors for RGS 1 and RGS 2 were derived from the relative intensities of Mkn 421 first and higher orders as shown in Fig. 4. The largest differences are at low wavelengths, where the effective area is small and a steep function of wavelength. It should be emphasised that such efficiency adjustments do not affect the better resolution of the higher orders which can be useful for the identification of lines or the resolution of blends.

2.1.7 Time and wavelength-dependent correction

In addition to the effects discussed in the previous paragraphs, during the last years there have been increasing evidences for a systematic discrepancy between the fluxes derived from RGS 1 and RGS 2.

Kaastra et al. (2018) [15] have derived a time and wavelength-dependent empirical correction to the

effective area to take into account this trend. After application of this correction the accuracy of the first order effective areas is 1-2% over most of the wavelength band. Also, there is a substantial improvement in the calibration of the second order.

This correction, applicable to data taken until February 2019, has been incorporated into the `EFFAREACORR` CCF and, as of SASv19, it is the default option in the generation of the response matrices with SAS (see [14] for details).

Observations taken in the last few years have shown indications of a decrease in effective area that cannot be explained by (only) an increase in the thickness of the Carbon contamination layer. Work is on-going to understand the reason for this loss of effective area and, eventually, take it into account in the calibration.

The RGS effective area in an observation is a result of the combination of all the considerations discussed above and thus is a complicated function of time, wavelength and source geometry. The quality of the RGS calibration is best judged by the success of the resulting models in two types of comparison: reproducing the known spectra of calibration standards, and the level of agreement with EPIC on calibration standards and a variety of other objects whose spectra are not known *a priori*. Detailed comparisons of this type using a large sample of observations throughout the mission are described in the XMM-Newton Cross-Calibration Status document [16].

2.2 Line spread function

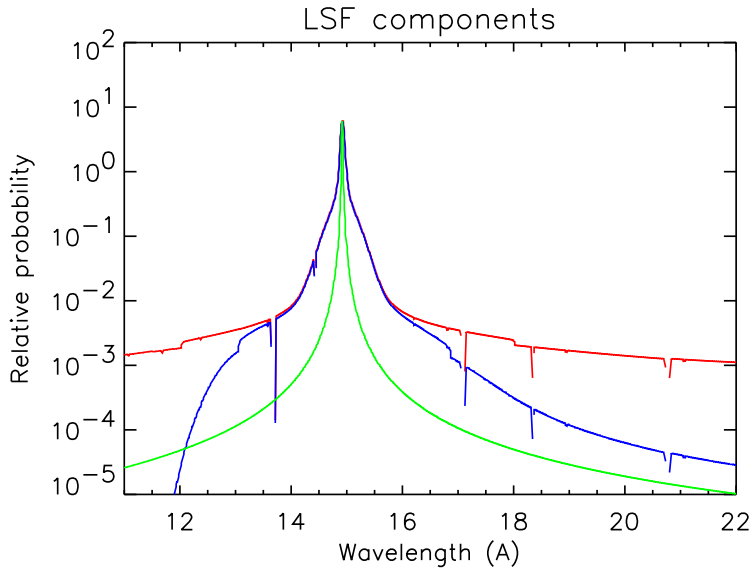

Figure 5: The three main components of the line response (LSF) of the RGS to a monochromatic line at 15 Å: the projected mirror response is shown in green; after broadening by the grating response in red; and after application of the energy selections to reduce the wings in blue. The small discontinuities are due to the approximation used in the numerical treatment of the small-angle scattering.

The monochromatic response, known as the line spread function (LSF), results from successive

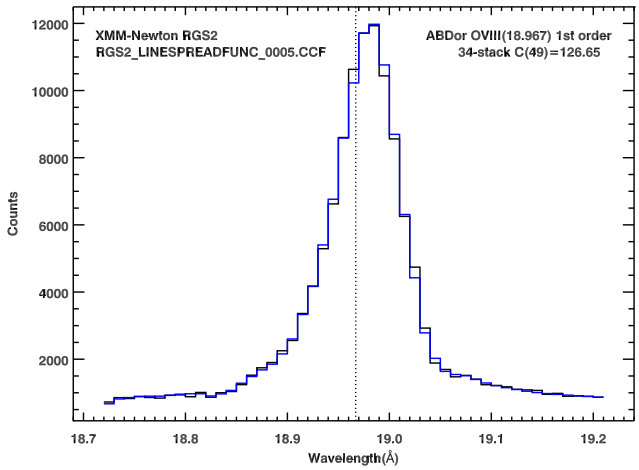

Figure 6: The O VIII Lyman α line of the active star AB Dor in RGS 2 first order spectra, showing stacked data in black and narrow-line model in blue from 34 observations spread through the mission. The observed width is of instrumental origin. The vertical dotted line shows the laboratory wavelength. C shows the C-statistic of the fit of the stacked model to the stacked data with the number of degrees-of-freedom in brackets.

convolutions of the mirror response projected in the dispersion direction, the grating response, and the detector response. The mirror response is approximated by a Lorentzian profile and was calibrated against the flight data of PKS 0312-770 in orbit 57 [17].

Different components contribute to the grating response:

- Accuracy of the variable line density
- Figure errors
- Misalignments between individual grating elements
- X-ray scattering by surface roughness

Two scattering components have been identified corresponding to different scales of the surface roughness: a small-angle Gaussian component and a large-angle Lorentzian component. This scattering is mainly a function of β, the outgoing angle from the gratings in the dispersion direction, but has also a component in cross-dispersion angle. For each order, β is related to wavelength through the diffraction equation:

$$\mathrm{m}\ \lambda = \mathrm{d}\ (\cos\beta\text{-}\cos\alpha)$$

where α is the incident angle on the gratings and d is the line spacing. The LSF components in the dispersion direction are illustrated in Fig. 5 where small-angle scattering causes the additional broadening at a few percent of the peak intensity and large-angle scattering dominates at larger distances from the core. Finally, the wings in the line-spread function were reduced by applying an energy selection in the CCD response. The effect of this selection is asymmetric as can be seen in the figure.

The LSF was compared early in the mission with lines observed in a number of stellar coronnae with agreement between model and data after modification of the instrument model to include a scaling

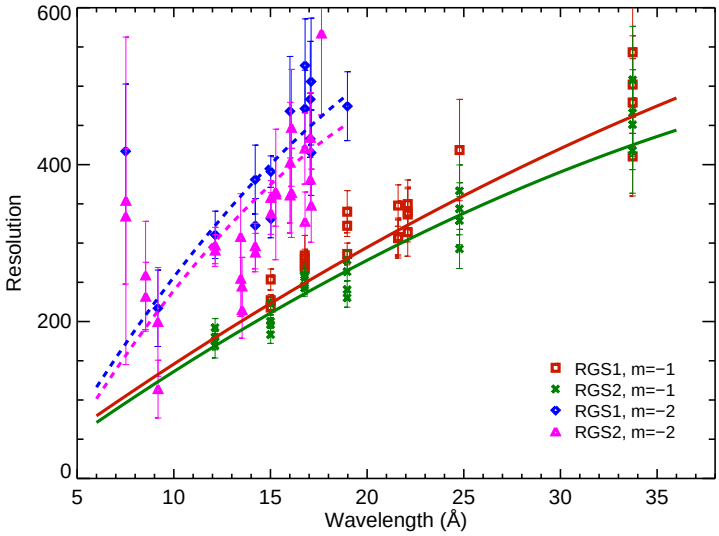

Figure 7: Comparison of measured (points) and modelled (lines) RGS 1 and RGS 2 spectral resolution for first and second order. The data are measurements of the width of a number of strong and relatively isolated emission lines of stellar coronnae [1].

factor applied to the pre-flight grating misalignment distribution of RGS 1. This forms the basis for the RGS response matrices calculated by the SAS and for the comparison of observed and predicted line profiles. Changes made in 2011 to the LSF models improved the description of the sharp core seen in strong lines [18]. Fig. 6 shows an example fit to a coronal O VIII 18.967,18.973 Å line.

Although several components of differing angular scales contribute to the complex shape of the LSF, the FWHM gives a rough measure of the instrument's performance. The empirically-determined width of strong, relatively isolated emission lines observed in coronal spectra is a slowly-varying function of wavelength in both RGS 1 and RGS 2 with mean FWHM of about 70 mÅ in first order and 50 mÅ in second order giving a spectral resolution that increases with wavelength with typical values of a few hundred (Fig. 7). It is estimated that an observed line broadening of more 10% of the FWHM can be considered to be significant for strong lines.

To give a concrete example, Fig. 8 shows data around a coronal Ne IX He-like triplet, showing the ability of the RGS to resolve these lines. At longer wavelengths, the He-like triplets of O VII and N VI are comfortably resolved. At shorter wavelengths, Mg XI and Si XIII are more difficult to separate.

2.3 Wavelength scale

The wavelength scale is determined by the geometry of the various instrument components. While the relative positions of the nine individual CCDs in each RGS instrument are known to high accuracy from measurements made during instrument integration, the overall instrument orientation and position of the camera reference points were subject to verification in flight using measurements of strong emission lines [19]. Subsequent work using many more lines in more observations has confirmed these measurements, allowed an accurate assessment of the misalignment between RGS 1 and RGS 2 [20, 21] and enabled a correction to the wavelength scale dependent on the angle between the Sun and the pointing direction of the spacecraft [22]. After these adjustments, the wavelength

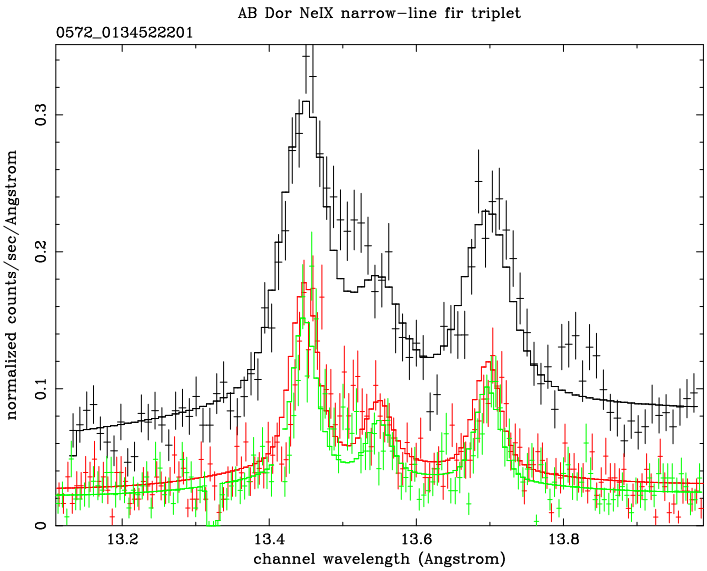

Figure 8: RGS spectra of AB Dor near the Ne IX *fir* triplet showing data and errors from RGS 2 first order in black and the higher-resolution second orders of RGS 1 and RGS 2 in red and green, respectively. The solid lines show a simple model of a narrow-lined triplet and continuum. The excesses near 13.5 Å and 13.8 Å are due to Fe XIX, which was not included in the model.

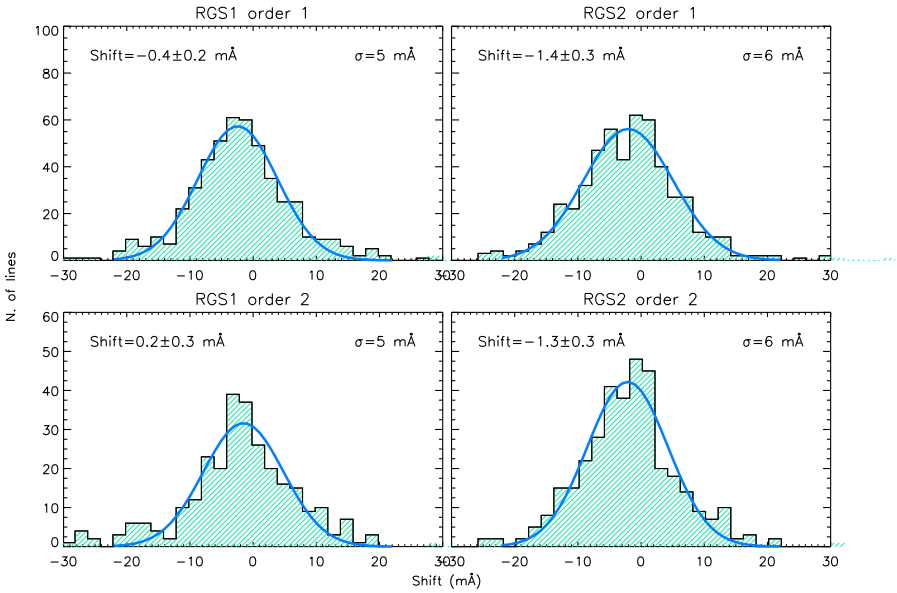

Figure 9: Shift between observed and laboratory wavelengths of a variety of narrow lines from measurements throughout the mission of several stellar coronnae in first and second order for RGS 1 and RGS 2.

scale shows rms residuals of 6 mÅ as shown in Fig. 9.

As a rule of thumb, every 1 arcsecond error in source coordinates causes a systematic error of up to 2.3 mÅ in the wavelength scale, emphasising the importance of using as accurate positions as possible in data analysis.

2.4 Cross-dispersion distribution

The distribution in the orthogonal cross-dispersion direction is somewhat different from the optimum mirror PSF as the detector follows the Rowland circle in the dispersion direction, which is not ideal for the mirror response, so an empirical determination is made instead. The cross-dispersion distribution of the smooth continuum of the X-ray bright blazar Mkn 421 has been parametrised [23] as a function of the dispersion angle β. This distribution is important as it provides the basis for the SAS to determine selection regions during calculation of point-source spectra.

2.5 RGS temporal resolution

The instrument time resolution in spectroscopy mode is determined by the CCD readout procedure. In double-node readout for RGS one CCD is read out every 0.5741 s, although this sometimes can reach 0.61 s; the full set of eight CCDs then takes about 4.8 s, which is thus the integration time of an individual CCD and the figure that best describes the instrument's temporal resolution.

In August 2007, the way in which RGS 2 is operated was changed. For several years, RGS 2 had been subject to occasional electronics problems with a current limiter during activation at the beginning of some orbits that caused a delay in switching the instrument to its normal spectroscopy mode. Because of the increasing frequency of this condition the decision was made to change the CCD read-out method in RGS 2 from double-node, in which data from the two halves of the chips are retrieved separately, to single-node, in which data from the whole chip are read out in through a single amplifier.

As the single-node readout takes twice as long, RGS 2 frame times are correspondingly twice as long as those from RGS 1, giving a CCD integration time of 9.6 s.

The consequences for pile-up of bright sources is discussed below in Sect. 3.2.

3 Calibration-related aspects of RGS data analysis

3.1 RGS Background

In the instrumental background various components have been identified due to:

- Minimum ionising particles
- Low-energy electrons
- Fluorescence lines from the housing
- Soft protons entering through the mirrors
- Calibration sources
- Read-out noise

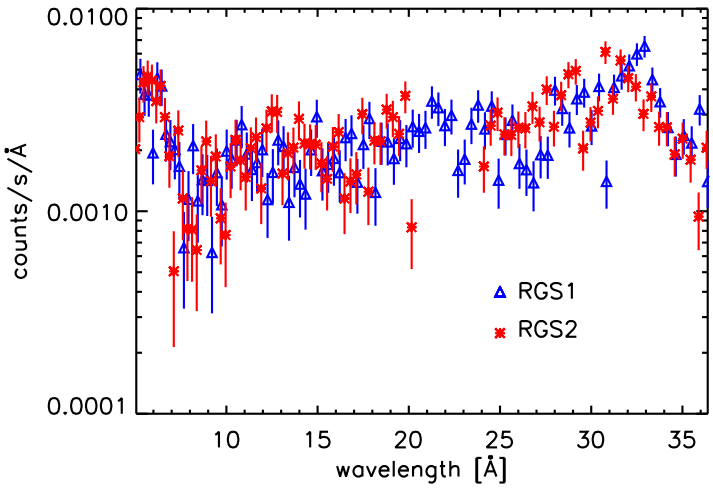

Figure 10: Count rate for the data selections {first order, 90% in CCD pulse height, all cross-dispersion angles} for a quiet part of an observation of the Lockman Hole

The net effect of this background can be illustrated using data from the Lockman Hole field which is blank for the RGS. The data shown in Fig. 10 were integrated over the *full* cross-dispersion direction of the detector for periods of a low soft-proton background. In general for point sources, the background can be reliably estimated from parts of the detector in the cross-dispersion direction outside the source-selection region, taking care to exclude the on-board calibration sources which illuminate parts of the CCDs. The locations of these calibration sources were chosen to interfere minimally with astronomical data. For extended sources, which can cover an arbitrarily large fraction of the detector's 5 arcmin cross-dispersion width, background region may be selected by inspection or independently by using blank-field RGS background template files [24, 25].

It is important to point out that the background is sometimes highly variable. It tends to be strong near the beginning and end of the spacecraft orbit due to the radiation belts but also to suffer at other times from a highly variable and even overwhelming contribution from soft protons due to solar events. It is recommended to use events in CCD9, which is closest to the optical axis, as a monitor to select for processing Good Time Intervals of low particle background. Readers are referred to [26], which discusses the evolution of the RGS background along the mission, and is regularly updated.

3.2 Pile-up

Pile-up is a familiar effect when observing bright X-ray sources with the EPIC instruments, which are non-dispersive and concentrate events from a point source within the small area of the focal plane covered by the PSF. Pile-up occurs when two or more photons are detected in the same pixel during the same integration, in which case they become combined into a multiple event. This can also happen in the RGS for very bright point sources when, e.g. two first-order events arrive in the same pixel close enough in time to be combined into a single apparent second-order photon. The introduction of RGS2 single-node operations discussed above in Sect. 2.5 with its longer read-out time has worsened the effect in RGS 2. As each RGS pixel suffers a level of pile-up dependent on its individual illumination, it is wise to consider separately line-rich and smooth-continuum sources.

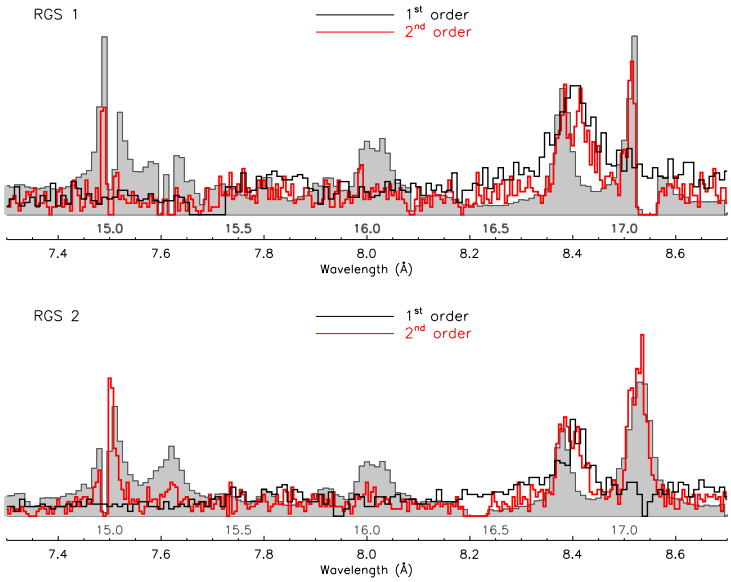

Figure 11: Short wavelength part of a spectrum of Capella taken after the introduction of the RGS 2 Single Node Readout mode in August 2007 (top: RGS 1, bottom: RGS 2). The first order spectrum is plotted in black and the second order in red. The grey-shaded histogram (with its wavelength scale show in grey as well) is the first order spectrum at double the wavelength. The second order spectrum is clearly contaminated by pile-up of the strong lines from the first order (Fe XVII 15.02, 16.78,17.05 Å), that show up as spurious features at half the wavelength ($\approx$ 7.5, 8.4 and 8.5 Å), and are not present in the first order spectrum. The effect, though present, is much less severe in RGS 1 than in RGS 2 due to the shorter readout time.

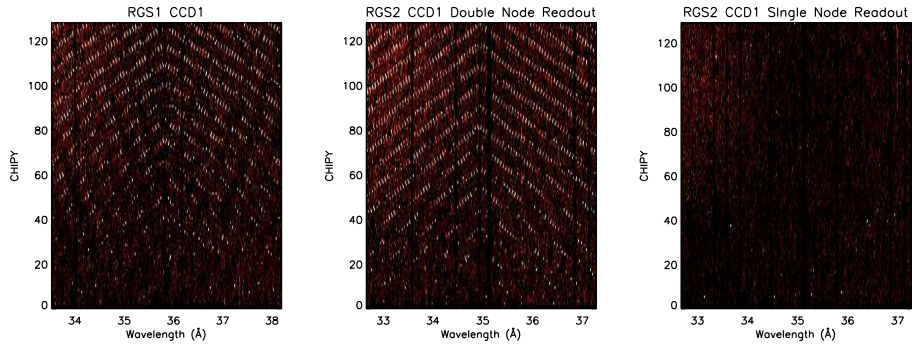

Figure 12: Example of Fixed Pattern Noise in CCD1. Left: RGS 1, centre: RGS 2 in Double Node Readout mode, right: RGS 2 in Single Node Readout (SNR) mode. The RGS 2 SNR mode is used in operations since August 2007.

Fig. 11 shows the strongest lines in the spectrum of Capella in the second order of RGS 2 at half their wavelength. Capella is one of the brightest X-ray sources in the sky with a high line-to-continuum ratio so this is more a worst case than a typical example. In the context of the RGS Small Window mode, specifically designed for bright sources, detailed comparison of first and second order spectra of Capella showed that pile-up losses amount to a few percent in the brightest lines [27].

For smooth-continuum sources, the pile-up fraction reaches about 2% for CCD count rates of 12 cts s^{-1} in RGS 1 and 6 cts s^{-1} in RGS 2. In the rare cases when sources are bright enough for a significant level of pile-up to have occurred, it is not an easy problem to treat, although in the worse cases of which we are aware in the brightest X-ray binaries the pile-up fraction was below 8%.

3.3 CCD detector defects

Removal of hot pixels and hot columns is a vital part of data analysis, as even a cursory glance at an unfiltered RGS event list will show. While this routine part of the SAS data analysis is usually quite successful, warm or cool - as opposed to hot - pixels that flicker occasionally are sometimes more difficult to detect. Especially for low-intensity sources this may result in distortions of the spectra that, nevertheless, can easily be identified. They are much narrower than the LSF and do not occur in both spectrometers at the same wavelength. In order to enhance the ability to distinguish sometimes subtle absorption or emission spectral features in cosmic sources from detector defects, the RGS offers the Multi-Pointing Mode [3] in which a series of spacecraft repointings are executed automatically in order to move detector blemishes to different parts of the spectrum.

3.4 Pixel offset values

In common with other CCD detectors, offset values are needed to calculate the energy of each detected RGS event. Early in the mission, a single offset value was used for each CCD node. Since SASv6 in 2004, an improved method uses dynamic values calculated for each individual pixel from diagnostic data averaged over three XMM-Newton revolutions [28]. These data are supplied with the ODF and used in RGS data reduction by the SAS with the default switch `withdiagoffset=yes`.

3.5 Fixed Pattern Noise

At long wavelengths (low CCD numbers) high-frequency noise can be visible due to so-called Fixed Pattern Noise in the detector that gives an unmistakable spatial modulation (Fig. 12). Since the introduction of single-node operations, Fixed Pattern Noise in RGS 2 has decreased considerably.

References

[1] Calibration and in-orbit Performance of the Reflection Grating Spectrometer on board XMM-Newton, A&A, 573,128, de Vries, C. et al., 2015.

[2] The Reflection Grating Spectrometer on board XMM-Newton, A&A, 365,L7, den Herder, J.W. et al., 2001.

[3] XMM-Newton User's Handbook

[4] http://www.cosmos.esa.int/web/xmm-newton/current-calibration-files

[5] RGS blazar spectra and prospects for an Effective Area correction, XMM-SOC-TN-0063, Pollock, A., 2004

[6] Effective area calibration of the Reflection Grating Spectrometers of XMM-Newton. I. X-ray spectroscopy of the Crab nebula, A&A, 497, 291, Kaastra, J., de Vries, C., Costantini, E. and den Herder, J.W., 2009

[7] An improved model the RGS effective area based on the build-up of carbon contamination, XMM-CCF-REL-238, Pollock, A., 2007

[8] The RGS effective area incorporating exponential contamination and a mechanism for rectification, XMM-CCF-REL-262, Pollock, A., 2010

[9] Correcting RGS Quantum Efficiency calibration defects, XMM-CCF-REL-108, Gabriel, C., 2002

[10] RGS 2 CCD2 Thickness of SiO_2 Layer, XMM-CCF-REL-71, Erd, C., 2001

[11] The interstellar Oxygen-K absorption edge as observed by XMM-Newton. Separation of instrumental and interstellar components, A&A, 404, 959, de Vries, C.,den Herder, J.W., Kaastra, J., Paerels, F., den Boggende, A., Rasmussen, A., 2003

[12] Tuning RGS Instrumental MgF_2 Absorption with Mkn 421, XMM-CCF-REL-212, Pollock, A., 2006

[13] RGS individual CCD sensitivities and 2nd and 3rd order grating efficiencies, XMM-CCF-REL-215, Pollock, A., 2006

[14] Update of the correction to the RGS Effective Area, XMM-CCF-REL-371, González-Riestra, R., 2019

[15] Effective Calibration of the RGS, XMM-SOC-TN-0219, Kaastra, J., de Vries, C., den Herder, J.W., 2018

[16] Status of the XMM-Newton Instrument Cross-Calibration, XMM-SOC-TN-0052, Stuhlinger, M. et al., 2010

[17] XRT PSF Parameterization for RGS, XMM-CCF-REL-63, Erd, C., 2001

[18] Modification of the RGS line-spread function, XMM-CCF-REL-275, Pollock, A., 2012

[19] The RGS Wavelength Scale, XMM-SOC-TN-0041, Lorente, R., Pollock A. and Gabriel, C., 2003

[20] The RGS Wavelength Scale, XMM-SOC-TN-0079, Coia, D. and Pollock, A., 2007

[21] Alignment of the RGS 1 and RGS 2 Wavelength Axes, XMM-SOC-TN-0080, Coia, D. and Pollock, A., 2008

[22] Sun-angle correction to the RGS wavelength scale, XMM-CCF-REL-297, González-Riestra, R., 2013

[23] RGS Cross-Dispersion PSF, XMM-CCF-REL-114, Gabriel, C., 2002

[24] RGS Background Spectra Templates, XMM-CCF-REL-229, González-Riestra, R., 2007

[25] Templates for the RGS Background, XMM-SOC-TN-0058, González-Riestra, R., 2004

[26] The Behaviour of the XMM-Newton Background, XMM-GEN-TN-0014, González-Riestra, R. and Rodríguez-Pascual, P., 2020

[27] RGS small window mode, XMM-SOC-TN-0086, Pollock, A. and Díaz-Trigo, M., 2010

[28] System offsets using diagnostic images, XMM-SOC-TN-0046, de Vries, C., 2003